



Article

Hybrid Compliant Musculoskeletal System for Fast Actuation in Robots

Pieter Wiersinga¹, Aidan Sleavin^{2,3}, Bart Boom^{2,3} , Thijs Masmeijer^{2,3}, Spencer Flint^{2,3} and Ed Habtour^{2,3,*}

¹ Faculty of Science and Engineering, University of Groningen, Postbus 72, 9700 AB Groningen, The Netherlands

² Department of Aeronautics & Astronautics, The University of Washington, Seattle, WA 98195, USA

³ The Illimited LAB, University of Washington, Guggenheim 211, Seattle, WA 98195, USA

* Correspondence: habtour@uw.edu

Abstract: A nature-inspired musculoskeletal system is designed and developed to examine the principle of nonlinear elastic energy storage–release for robotic applications. The musculoskeletal system architecture consists of elastically rigid segments and hyperelastic soft materials to emulate rigid–soft interactions in limbless vertebrates. The objectives are to (i) improve the energy efficiency of actuation beyond that of current pure soft actuators while (ii) producing a high range of motion similar to that of soft robots but with structural stability. This paper proposes a musculoskeletal design that takes advantage of structural segmentation to increase the system’s degrees of freedom, which enhances the range of motion. Our findings show that rigid–soft interactions provide a remarkable increase in energy storage and release and, thus, an increase in the undulation speed. The energy efficiency achieved is approximately 68% for bending the musculoskeletal system from the straight configuration, compared to 2.5–30% efficiency in purely soft actuators. The hybrid compliance of the musculoskeletal system under investigation shows promise for alleviating the need for actuators at each joint in a robot.



Citation: Wiersinga, P.; Sleavin, A.; Boom, B.; Masmeijer, T.; Flint, S.; Habtour, E. Hybrid Compliant Musculoskeletal System for Fast Actuation in Robots. *Micromachines* **2022**, *13*, 1783. <https://doi.org/10.3390/mi13101783>

Academic Editor: Joseph A. Potkay

Received: 14 September 2022

Accepted: 17 October 2022

Published: 20 October 2022

Publisher’s Note: MDPI stays neutral with regard to jurisdictional claims in published maps and institutional affiliations.



Copyright: © 2022 by the authors. Licensee MDPI, Basel, Switzerland. This article is an open access article distributed under the terms and conditions of the Creative Commons Attribution (CC BY) license (<https://creativecommons.org/licenses/by/4.0/>).

Keywords: nature-inspired; robots; nonlinear; dynamics; biomimetic; antagonistic actuation; energy storage–release

1. Introduction

It is quite remarkable to witness the massive scientific advancements in the field of biomimetic and soft robots just in the last decade [1–5]. Significant research has focused on engineering various compliance mechanisms to enable adequate soft actuation for nature-inspired robots [6–10]. Through compliance, i.e., high elastic deformation, soft actuation is achieved by distributing the loads to minimize interfacial stress concentrations [11,12]. Often, soft actuators are comprised of novel active materials and complex auxiliary circuits. Utilizing 3D printing, a variety of active materials can be leveraged, such as hydrogels [13], conductive polylactic acid [14], shape-memory alloys [15], and multiphase materials [16]. The auxiliary circuits can be thermal [16], fluidic [17], magnetic [18], or electrical [6]. Realizing soft robots into practical applications is still lagging due to performance shortcomings of their compliant mechanisms, such as low energy efficiency [19] and structural stability when bearing high loads [20,21].

Responding to these shortcomings, we introduce in this study a nonlinear hybrid compliant mechanism into a snake-inspired musculoskeletal architecture [22]. The aim is to depart from purely soft or rigid actuation to combined rigid–soft interfaces, as shown in Figures 1 and 2. The hybrid compliant mechanism allows us to maintain rotational synchronous motion [23] at the joints by taking advantage of bidirectional antagonistic stiffness actuation [23] instead of using rigid bidirectional servo motors or purely soft actuators, which are often seen in biomimetic robots [24–26]. Antagonistic variable stiffness actuation was achieved by placing the continuum soft (hyperelastic) materials in

opposing directions to the neutral axis position for torque production about the joint (see Supplementary Materials Video S1). Hybrid compliant mechanisms are advantageous for generating high energy storage–release because they can produce a large range of motion and geometric and material nonlinearities simultaneously (Figure 2a–c) [22], as described in Sections 1.1 and 1.2. The nonlinearities are due to the high elastic stretch in hyperelastic materials, which is key to increasing strain energy storage. The antagonistic hybrid compliant design approach accomplished two objectives: (i) improving the energy efficiency for actuating undulations over current soft actuators and (ii) producing a high range of motion while maintaining structural stability. The energy storage–release principle was demonstrated analytically and experimentally for planar undulation only (Figure 2d).

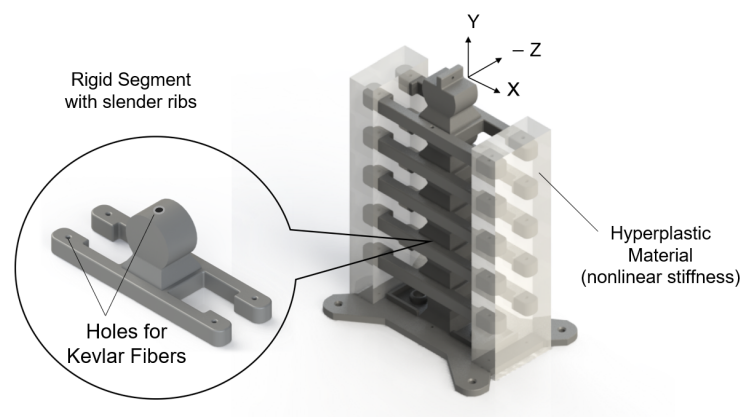


Figure 1. The snake-inspired musculoskeletal system consists of rigid segments (dark gray) connected with hyperelastic material (transparent sections) at the end of the ribs. Each rigid segment has a socket–disk joint and two ribs on each side. The hyperelastic material provided nonlinear elastic energy storage. The ribs transfer energy between the $-X$ and X sides.

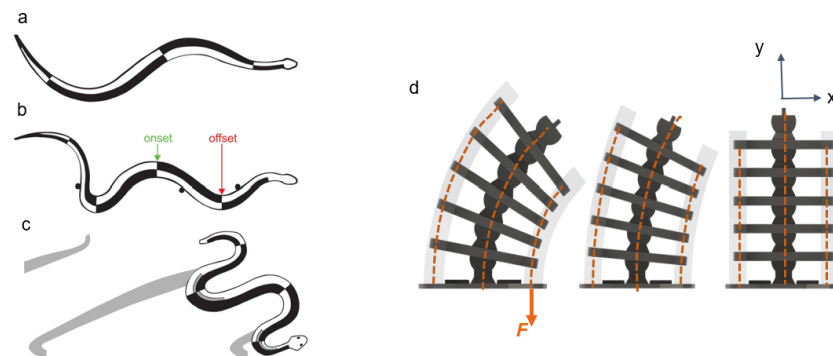


Figure 2. (a–c) Undulations in snakes [22]: the black-shaded areas are the muscle timing relative to bending in (a) swimming and (b) lateral undulation of a water snake and (c) sidewinding in a rattlesnake. The outside gray areas are past regions of static contact with the ground; note the onset and offset bending points. (d) Bends in our snake-inspired system: the transparent sections are the hyperelastic (soft) material connecting the ribs and providing antagonistic variable stiffness and energy storage–release. Kevlar fibers in the soft material and centerline provide actuation and prevent socket shifting, respectively.

1.1. Nonlinear Hybrid Compliance

Our system is designed to be nonlinear hybrid compliant, a subclass of compliant mechanisms that combines geometric and material nonlinearities [27–31]. Their influence on storing and releasing strain energy in biological and robotic musculoskeletal systems is underexplored [32–34]. Through reliance on flexible instead of rigid components, compliant mechanisms can sustain large elastic deformations to realize both high mobility and energy storage. Figure 3 provides three compliant approaches: springs, flexible structures [35],

and nonlinear materials[36]. When selecting commercially available linear and nonlinear springs, designers are limited by their coiled architecture, space requirements, and force–displacement range (Figure 3a).

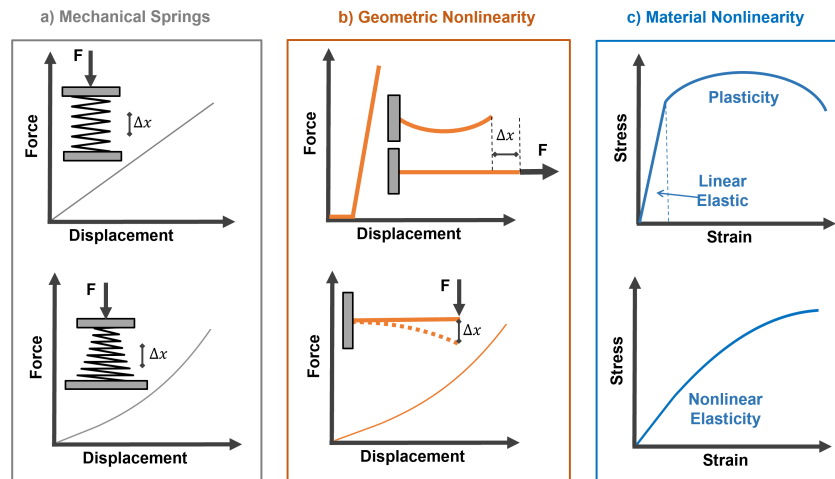


Figure 3. (a) Force–displacement response for linear (top) and nonlinear (bottom) conical springs, where F is the applied force, and Δx is the displacement; (b) examples of geometric nonlinearity in slack–tension (top) and bending (bottom) structural members; and (c) stress–strain in materials exhibiting elastoplasticity (top) and nonlinear elasticity (bottom).

The geometric nonlinearities of flexible structural elements offer an attractive alternative to conical springs. They can reach high deformation before the materials exhibit any significant departure from the linear stress–strain regime [37]. Examples of nonlinear force displacement due to slack–tension and bending of flexible structures are illustrated in Figure 3b. Common material nonlinearities ranging from elastoplasticity to nonlinear elasticity are shown in Figure 3c. Materials operating in nonlinear elastic regimes have higher strain-energy storage than linear ones, as shown in Figure 4. For a musculoskeletal design, distributed nonlinear hybrid compliance can be achieved by combining the geometric and material nonlinearities (Figure 4). In this study, the principles were demonstrated for linear and softening regimes.

1.2. Musculoskeletal Energy Storage–Release

Variable stiffness, which is the inverse of compliance, is directly related to its exploitation of strain energy: the area under the stress–strain or force–displacement curve. In this study, the soft continuum was hyperelastic material, where the stress–strain was nonlinear elastic (also known as dynamic softening) [38–40], as shown in Figures 3c and 4b.

Hardening can be achieved through geometric nonlinearities and is key for increasing the speed of return (snap) from the deformed state to the neutral position upon releasing the stored bending energy. The stored elastic energy was released rapidly at ~ 22 ms. The musculoskeletal system achieved $\sim 68\%$ energy efficiency for executing high bending motion from a straight configuration to a 158 mm radius. Our energy efficiency exceeded that of soft actuators reported in the literature, which ranged from 2.5% to 30% [41–43]. The nonlinear compliance of the musculoskeletal system allowed us to eliminate the need for mechanical motors at the joints by leveraging the moments applied at the ribs.

The musculoskeletal system design and fabrication are presented in Section 2. The kinematics of the segmented system are detailed in Section 3. Section 4 describes the experimental setup and the approach for evaluating energy storage–release. The theoretical development of elastic energy storage in hyperelastic materials is provided in Section 5. The experimental and analytical results are detailed in Section 6.

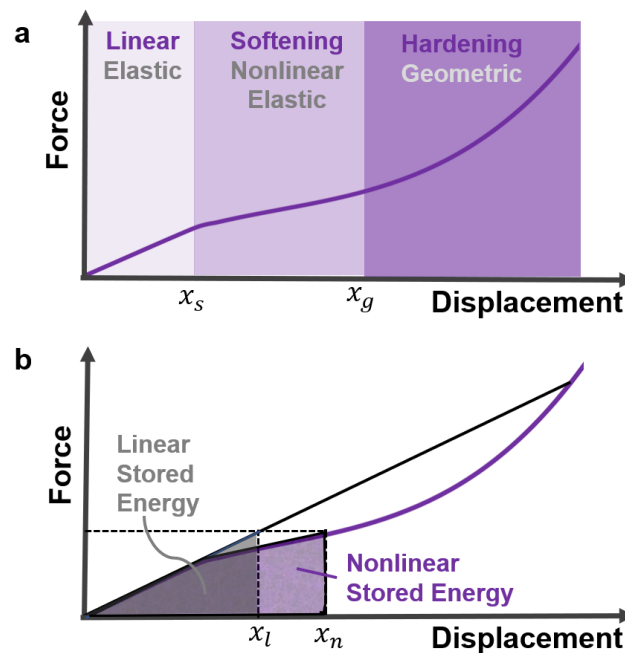


Figure 4. (a) Force–displacement curve of typical nonlinear hybrid compliance with linear softening (starts at x_s) and hardening (starts at x_g) stiffness regions; (b) note the linear and nonlinear displacements, x_l and x_n , respectively, for the same force. Thus, energy storage, the area under the curve, is higher in nonlinear (purple) than in linear (gray) hybrid compliance.

2. Design and Fabrication

The musculoskeletal system consisted of six 3D-printed rigid segments (Figure 1) connected with hyperelastic material and Kevlar fibers. The hyperelastic material held both sides of the rigid segments of the full musculoskeletal assembly near the rib ends in the $+X$ and $-X$ directions (Figure 2). Additionally, Kevlar fibers ran internally through the neutral line of the structure. The rigid segments were fabricated using polylactic acid (PLA) with 35.9 MPa tensile strength and 4% maximum elongation [44]. The hyperelastic material was platinum-catalyzed silicone Ecoflex 00-30 with $\sim 900\%$ rupture. The Kevlar 29 tensile strength was ~ 2.75 GPa [45].

The overall musculoskeletal system's height and width were 200 mm and 120 mm, respectively (Figure 5a). The dimensions of a rigid segment are provided in Figure 5b. Each rigid segment consisted of a disk–socket joint with two ribs on each side. The system's total mass was approximately 220 grams. All the rigid segments were allowed to rotate except for the bottom segment. The musculoskeletal system was attached to a rigid base metal plate to ensure a fixed boundary condition at the bottom segment.

Fused deposition modeling (FDM) was utilized to print each rigid segment separately using an Ultimaker II 3D printer with an 8 mm nozzle head. The rigid segments were 3D printed with PLA filament, a thermoplastic polymer material. It was necessary to 3D print the PLA material of the ribs along the directions of $+X$ and $-X$ to sustain the normal bending stresses induced by the resistive forces in the soft material [46].

The final assembly of the musculoskeletal system was achieved by submerging the rigid segments with Kevlar fibers in the hyperelastic material and then allowing them to cure. We selected Ecoflex for fabricating the soft material due to its flexible casing properties and low viscosity, which enabled us to obviate most of the air bubbles trapped inside the soft material via agitation before curing. The soft material was cured at room temperature, which eliminated any potential thermal expansion issues.

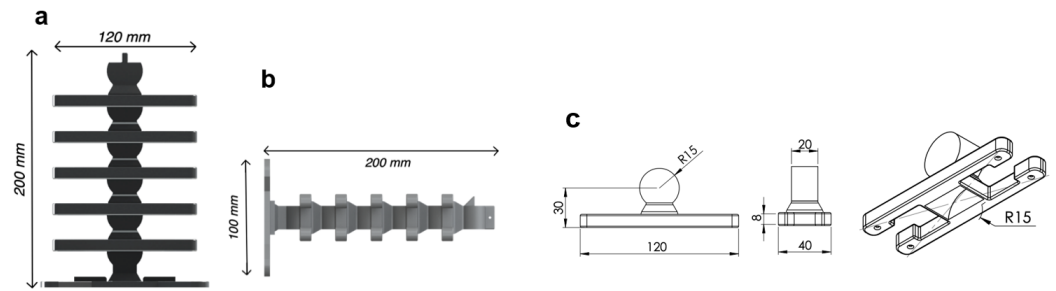


Figure 5. The musculoskeletal system consisted of six rigid segments: (a) front and (b) side views show the overall dimensions; and (c) shows the dimensions of a rigid segment, which consisted of four ribs. The fibers ran through holes in each segment to transmit the forces in hyperelastic material for actuation. The disk–socket joint enables rotation for undulation. The socket is the bottom cavity in the (c) isometric view.

The disk–socket joint design of the rigid segments permitted only tangential rotation, as shown in Figure 6. Inserting fibers through the neutral line of the rigid segments ensured that bending occurred only at the pivot points—located at the center of each rigid segment to simplify kinematic analysis [47]. This connection can be thought of as the spinal cord in the vertebrae.

Similar to a snake’s vertebrae, the rotation of each rigid segment induced the collective bending of the complete system, as shown in Figure 6. Therefore, the design strategy facilitated distributed actuation of the system through the soft material by simply applying tension forces carried by the fibers to rotate the rigid segments and cause stretch and contraction in the soft material. The material snapped back to an equilibrium state upon removing the tension forces—releasing the stored energy and returning the spine to the center line.

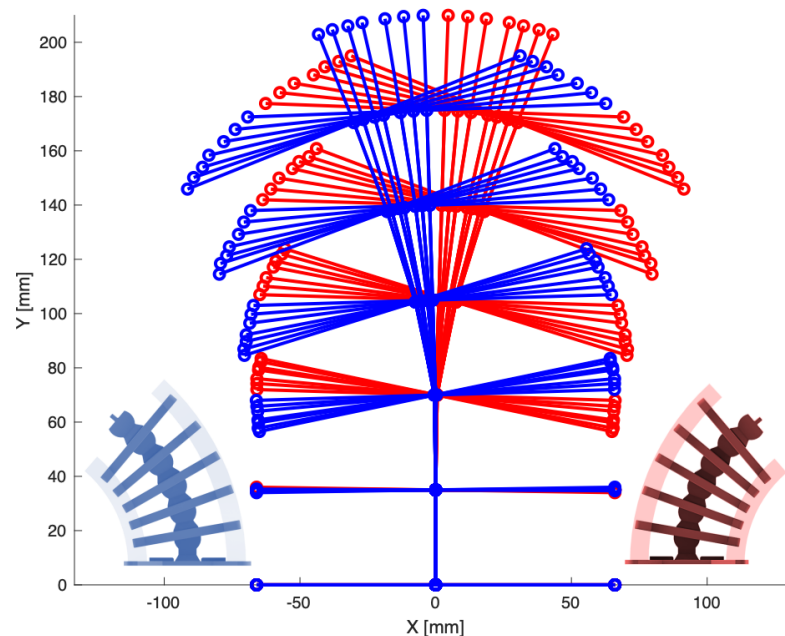


Figure 6. Using imaging analysis, displacements were obtained experimentally for each rigid segment at the center and at the rib endpoints (highlighted in markers). Right (+X) and left (−X) are shown in red and blue, respectively.

3. Kinematics Development

development of the kinematics required identifying the minimal degrees of freedom to describe the musculoskeletal system’s full motion. The undulation displacement for each segment n is expressed by the angle, θ_n , with respect to the horizontal axis, as depicted in Figure 7.

The angle γ in Figure 8 is of the fiber at the n th segment with respect to the vertical axis. The distance between pivot points n and $n - 1$ is b , which is fixed. The horizontal distance a is from a pivot point to the side fibers. The resultant length between ribs n and $n - 1$ is d . Due to the design symmetry of the system (Figure 8), the tip displacements of the n th rib at a can be calculated as follows:

$$\begin{Bmatrix} x_{rn} \\ y_{rn} \end{Bmatrix} = \begin{Bmatrix} x_{pn} \\ y_{pn} \end{Bmatrix} + a \begin{Bmatrix} \cos \theta_n \\ \sin \theta_n \end{Bmatrix} \tag{1}$$

where x_{pn} and y_{pn} are the pivot point displacements of rigid segment n rotating in the xy plane. The net angular displacement between segments n and $n - 1$ is:

$$\phi_n = \theta_n - \theta_{n-1} \tag{2}$$

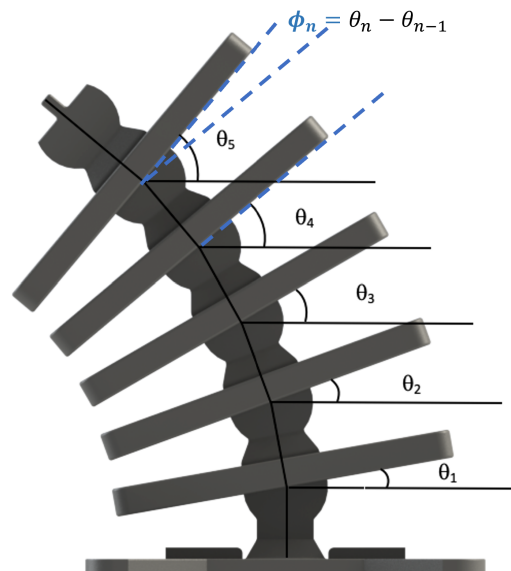


Figure 7. The angles θ_n are the degrees of freedom of the musculoskeletal system with respect to the horizontal axis. The bottom rigid segment is fixed. The angle ϕ_n is the displacement between segments n and $n - 1$.

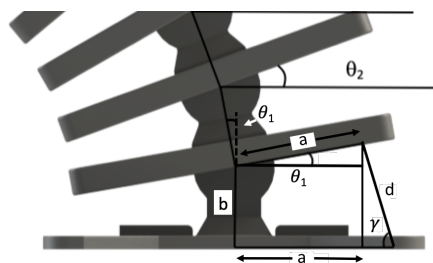


Figure 8. Local geometric parameters used to develop the kinematics.

4. Experimental Evaluation

Two sets of experiments were performed to evaluate the energy storage and release of the musculoskeletal system. Each experiment was conducted seven times to ensure repeatability. The first set examined the elastic energy capacity of the actuator by measuring the range of bending motion due to a vertical force applied to the side fibers running

through the ribs and a bending force at the maximum moment arm of the actuator, as shown in Figure 9a,b, respectively. In the second set, the musculoskeletal system was exposed to impulse forces, causing it to undulate. The system's structural damping and the linear and nonlinear structural stiffness were calculated in Section 5.

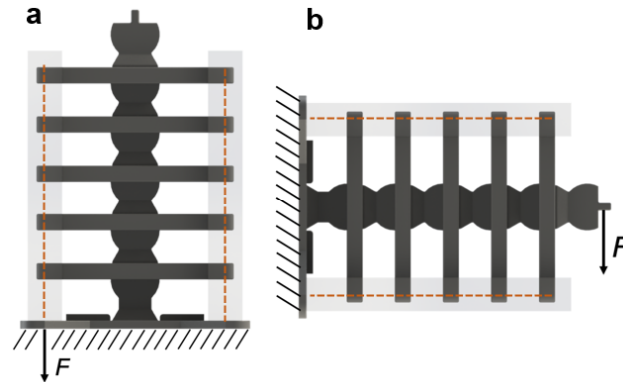


Figure 9. Loading configurations in the (a) vertical and (b) horizontal directions. F is the applied load. The orange dash lines indicate the internal fibers

The metal base of the musculoskeletal system was rigidly fixed to a test frame with four bolts. The test was constructed with 80/20 T-slot aluminum, as shown in Figure 10. The musculoskeletal system bending motion was recorded using a video camera (Model: HDR-CX405, SONY, Tokyo, Japan). The recording was set for a full high-definition option with 60 frames/second. Both the musculoskeletal system and camera were rigidly secured to the test frame to maintain accurate measurements.

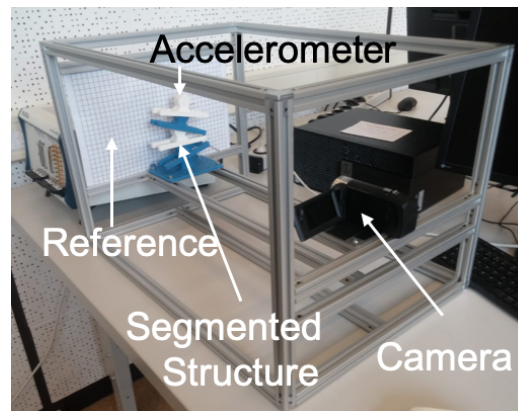


Figure 10. The musculoskeletal system and the video camera were secured to a rigid test frame to maintain accurate measurements. A scale reference was positioned behind the system to facilitate reference for the tracking software.

4.1. Energy Storage Assessment

Video-tracking software called Tracker was utilized to extract the displacement data from videos for each image frame [6]. An example video is provided as a Video S2. Bending displacement was achieved by applying force in the vertical configuration and then switching to the horizontal configuration by rotating the musculoskeletal system by 90° , as illustrated in Figure 9a,b, respectively. The maximum applied force was 29.4 N for both configurations.

Using Tracker, the pivot points were identified and collected for each video frame, as shown in Figure 11. The horizontal and vertical axes were specified in each frame with a scale reference. The displacement measurements were converted to data format files to facilitate kinematic analysis using a customized MATLAB—code provided in Code S3 File. The code calculated the change in the angle of every rigid segment relative to the horizontal

reference line for every frame, and the net angle, ϕ_n . The change in the distance d was obtained from the angle calculations. The change in distance d was utilized to calculate the stretch in the soft material, as detailed in Section 5.

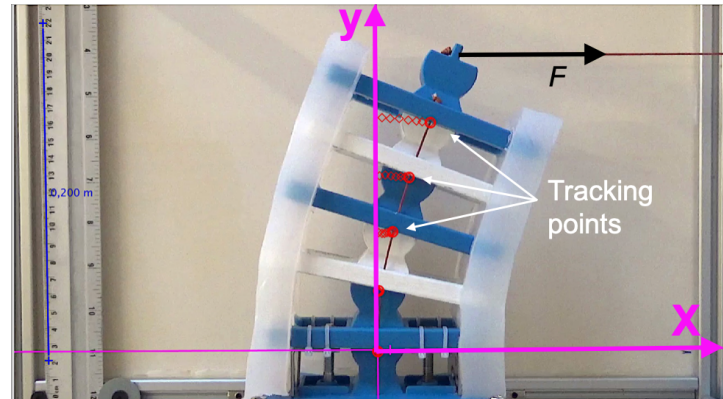


Figure 11. Image tracking of musculoskeletal system motion was obtained using an app called Tracking. The ruler on the left side was utilized for scaling the experimental images.

4.2. Energy Release Assessment

Assessing the energy release required obtaining dynamic parameters due to applying an impulse force, namely structural stiffness and damping. An acceleration sensor was utilized since the video camera lacked the required framerate needed to capture high-frequency undulations. Acceleration measurements were obtained using a lightweight (≈ 1.0 g) tri-axial sensor (5.0 mV/g sensitivity, Model 3133A3, Dytran Instruments, Inc., Chatsworth, CA, USA). The sensor was placed at the center of the top rigid segment of the system, as illustrated in Figure 10. The impulse force was delivered to the top segment in the horizontal direction (X) using a miniature modal hammer (21.1 mV/N sensitivity, Model 2302-100, Meggitt Endevco, Irvine, CA, USA). The sensor and impulse force placement at the top segment provided the most accurate measurements because the motion was maximum. The response was normalized by the input force.

5. Mechanics of Elastic Energy Storage–Release

5.1. Elastic Storage in Hyperelastic Material

It is assumed that silicone material behaves in an isotropic manner [36]. Based on the uniaxial nonlinear elastic deformation range, the stretch ratio in the axial direction can be calculated as follows:

$$\lambda_1 = \frac{l}{l_0} \tag{3}$$

The engineering strain is $\varepsilon = \lambda - 1$. The principal stretch is [48]:

$$J = \lambda^2 + \frac{2}{\lambda} \tag{4}$$

The silicone stress–strain response was obtained from uniaxial tension testing for three samples, as shown in Figure 12. Each sample was stretched up to 100% strain. The neo-Hookean model was applied to capture the soft-material deformation with reasonable accuracy (Figure 12). The neo-Hookean model is based on a strain-energy-density function given by the following expression [6]:

$$S = \frac{E_0}{6}(J - 3) \tag{5}$$

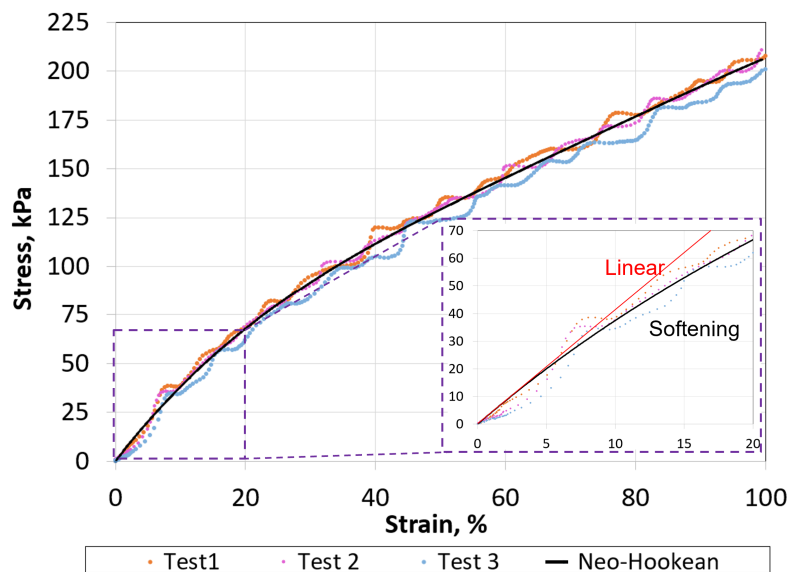


Figure 12. Neo-Hookean hyperelastic constitutive model shows good agreement with the experimental stress–strain response of the soft material. The inset plot shows the nonlinear response at low strains, which is the softening (black curve) region in Figure 4. The straight red line highlights the nonlinear response.

From Figure 12, the elastic constant at the initial stretch, E_o , was 3.602 MPa. Substituting J into S and differentiating with respect to λ , the uniaxial nominal stress becomes:

$$\sigma = \frac{E_o}{3} (\lambda - \lambda^{-2}) \tag{6}$$

Knowing $\sigma = E_e \epsilon$, the variable elastic modulus as a function of the stretch can be calculated as follows:

$$E_v = \frac{E_o}{3} \left(\frac{\lambda - \lambda^{-2}}{\lambda - 1} \right) \tag{7}$$

Each segment was approximated as a nonlinear rotational spring element, which was a concentrated variable-bending stiffness. Each rib displacement due to bending can be approximated as $\Delta x_n = a \sin \phi_n$, since ϕ_n is relatively small compared to the total displacement of the system. Therefore,

$$\lambda = \frac{l_o + a\phi_n}{l_o} \tag{8}$$

The overall bending displacement exhibited linear and nonlinear quadratic deformations. Therefore, the restoring force can be expressed as the combined effect of linear and nonlinear springs:

$$F_n = (k_{n,1} + k_{n,2}\phi_n)\phi_n = S_n\phi_n \tag{9}$$

where S_n is the equivalent nonlinear stiffness for the n th spring, as shown in Figure 13—the linear and nonlinear stiffness values are $k_{n,1}$ (spring without arrow) and $k_{n,2}$ (spring with arrow), respectively. Equation (9) was utilized as an analytical model to calculate the force–displacement for each segment n . The stored elastic energy U_n for the n th spring can be obtained by integrating the force in (9) with respect to the displacement [49]:

$$U_n = \frac{1}{2}k_{n,1}\phi_n^2 + \frac{1}{3}k_{n,2}\phi_n^3 = \left(\frac{1}{2}k_{n,1} + \frac{1}{3}k_{n,2}\phi_n \right) \phi_n^2 \tag{10}$$

The total elastic energy stored in the system can be computed by summing all U_n .

$$U_{total} = \sum_n U_n \tag{11}$$

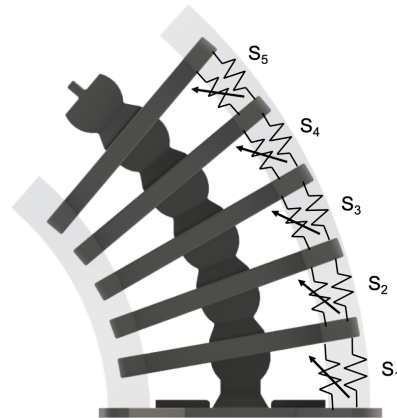


Figure 13. The soft material model was expressed as linear and nonlinear springs (S_n) using constant and tunable resistive elements, respectively.

5.2. Energy Release in Undulation

The entire system resonance frequency (f_r) and damping ratio (η) were obtained experimentally from the acceleration measurements after each impulse event from the frequency domain data. The resonance frequency can be thought of as the rate at which the musculoskeletal system will oscillate at its dominating mode shapes [50]. Bending was the first dominating mode shape, i.e., the mode with the lowest f_r . The undulation frequency is given by [51]:

$$f_r = \frac{1}{2\pi} \sqrt{\frac{k_e}{m_e}} \tag{12}$$

In the context of structural dynamics, the effective stiffness and mass for the first mode of the entire musculoskeletal system are k_e and m_e , respectively [52]. For clarity, the effective (or moving) mass is intrinsic to a mode shape and is not the same as the total mass of the system, since each part in the structure will move differently. Similarly, k_e is the effective stiffness of all components forming specific shapes for different harmonics. Additionally, η is the ratio of the energy dissipated, E_d , to the maximum elastic energy stored. Therefore, the total energy released for the entire system can be calculated as follows:

$$E_r = U_{total} - E_d = U_{total}(1 - \eta) \tag{13}$$

The damping ratio can be estimated at each resonance frequency from the amplification factor as follows [53]:

$$\eta = \frac{1}{2Q_r} \tag{14}$$

The amplification factor Q_r is computed using the half-power bandwidth method [53]:

$$Q_r = \frac{f_r}{\Delta f} \tag{15}$$

where Δf is the frequency bandwidth between -3 dB points on the frequency response function, also known as the half-power points. For additional interest in the method, the reader is encouraged to reference [53].

6. Results and Discussion

6.1. Elastic Energy Storage

The experimental and analytical range of motion, ϕ_n , due to the application of forces in the vertical and horizontal directions are provided in Figures 14 and 15, respectively. The experimental and analytical results are shown in markers and lines, respectively. The angle ϕ_n

and force F are expressed in degrees and N, respectively. The displacements were calculated using (9), where the force–displacement relationships included the material nonlinearity.

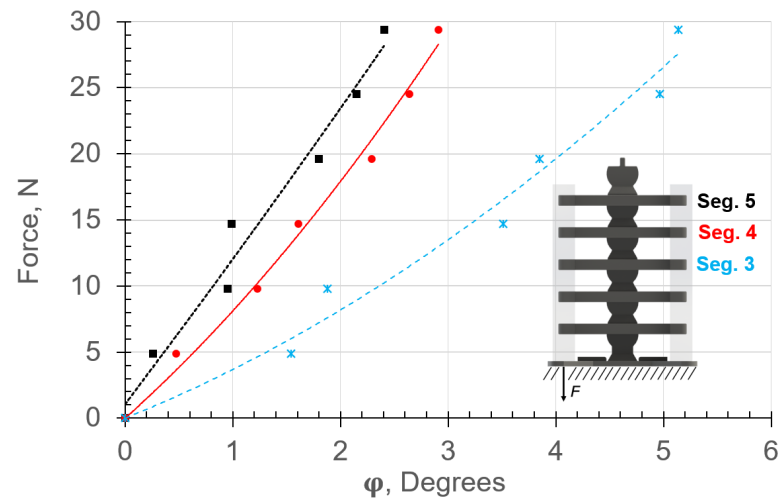


Figure 14. Force–response results for vertical loading obtained by applying force at the end of the left-side fibers. Experimental and analytical (from (9)) results are shown in markers and lines, respectively. Note the nonlinear bending behavior due to contraction of the soft material on one side and stretch on the other.

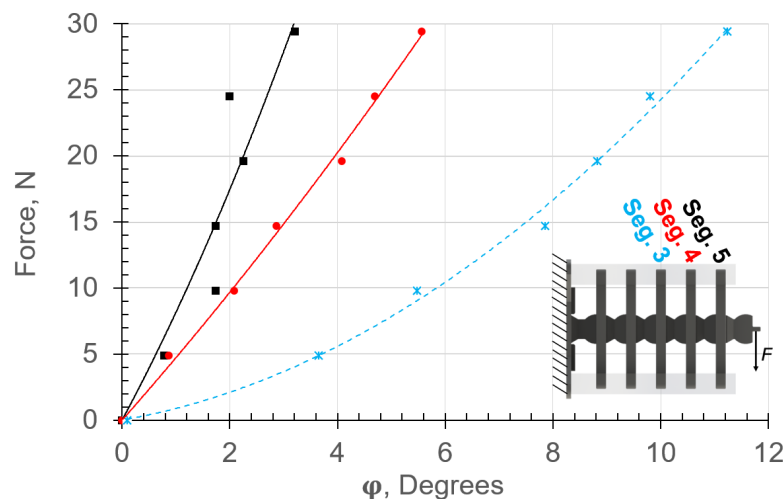


Figure 15. Force–response curves for horizontal loading obtained by applying force at the end of the top rigid segment. Experimental and analytical (from (9)) results are shown in markers and lines, respectively. Note the nonlinear bending behavior due to contraction of the soft material on one side and stretch on the other.

Inducing vertical and horizontal loads caused compression and tension stresses in the left and right soft muscles (Figure 6), respectively. It can be observed that the analytical results are in good agreement with the experimental data for both vertical and horizontal configurations (Figures 14 and 15, respectively). The displacement ϕ_n in both cases (Figures 14 and 15) differed for each rigid segment and was nonlinear except for Top Segment 5, which behaved linearly due to lower stretch/contraction in the soft materials. This expected behavior resembled nature because each soft muscle, S_n , between two rigid segments deformed differently. Hence, in biological musculoskeletal systems, the muscles tend to be thicker and highly stretchable in areas with high bending [9].

The nonlinear deflection behaviors were attributed to the hyperelastic material’s capability of aggregating significant elastic energy as a function of the large geometric displacement in the system. Notice the change in the resistance force in the spring segments

S_3 and S_5 as a function of ϕ_n . The highest nonlinear displacement occurred in the lowest soft element. The lower elements carried more bending loads than the top ones. Therefore, the maximum energy storage capacity occurred in the soft muscles (springs) closer to the base due to the high stretch on one side and compression on the other. Additionally, S_3 experienced dynamic hardening as the tension force was increased, while S_4 and S_5 experienced dynamic softening. The stretch in S_3 due to the horizontal loading configuration was higher than that for the vertical configuration. Since the moment arm in the horizontal loading configuration was higher than that in the vertical case, the stresses were higher as well.

Finite element analysis (FEA, using Abaqus CAE-SIMULA, Dassault Systemes, Vélizy-Villacoublay, France) was performed to gain additional insights into the elastic energy storage mechanics, as shown in Figure 16. The analysis was conducted for the horizontal loading configuration up to 29.4 N. We assumed that the rigid and soft materials were elastic, isotropic, and incompressible. However, the hyperelastic material constitutive model supplied to ABAQUS was based on the experimental stress–strain data in Figure 12. The effect of geometric nonlinearity was included in the model. Quadratic brick 20-node (C3D20) elements were utilized to mesh the rigid segments. For the hyperelastic material, 20-node quadratic brick hybrid (C3D20H) elements were chosen to remedy volume–strain locking due to the silicone’s high Poisson ratio of 0.48 [48]. Future FEA studies will be required to understand the effect of hysteresis on energy storage–release in the system over time.

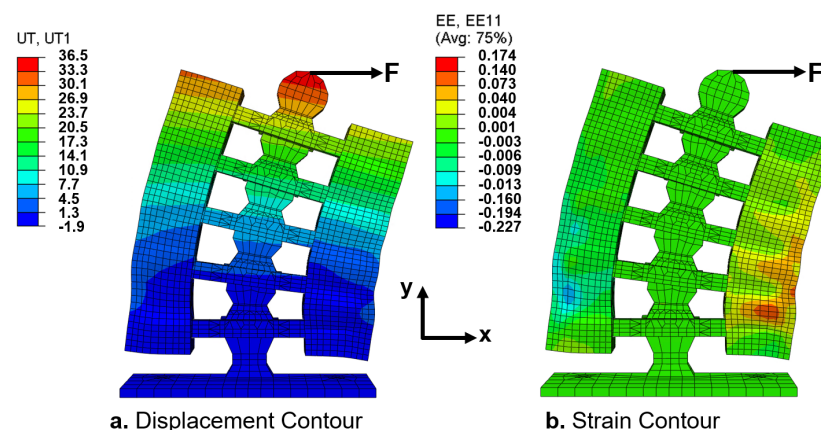


Figure 16. Contours of the displacement in the X-direction (a) and of the principle strain, ε_{xx} , due to a 29.4 N force applied to the end of the top rigid segment; (a) the maximum displacement (in mm) is $\phi = 11.0^\circ$, which is 4.4% less than the maximum experimental angle of 11.5° ; (b) the strain is highest in the hyperelastic materials between the rigid segments (ribs), where energy is stored.

The contours of the transverse displacement in the X-direction and principle strain, ε_{xx} , are reported in Figure 16 for the 29.4 N force (Figure 15). The maximum deflections obtained from the simulations were in good agreement with the experimental results. The largest error was $\sim 4.4\%$ at 29.4 N, where the FEA and experimental deflections were 11.0° and 11.5° , respectively (Figure 16). The deviation between the simulations and experiments could be attributed to the low geometric tolerances of 3D printing and silicone casting. Figure 16 shows that the tension and compression in the hyperelastic material were maximum and minimum between the lower and top ribs, respectively. For example, the strains in the stretched and compressed regions of the S_2 spring were approximately 17.4% and 22.7%, respectively. On the $-X$ side, the elastic stretch caused distributed strain in the nonlinear material from 2% to a maximum 22.7%, where substantial elastic necking occurred. Conversely, the strain in the compressive side was more distributive than that in the stretched side. This is common behavior in hyperelastic materials [48]. However, including compressive tests of the hyperelastic material may remedy the deviation between the FEA and experimental results.

Estimating elastic energy storage was achieved by calculating the forces required to restore the assembly to its equilibrium state, i.e., to the assembly's centerline. The total elastic energies stored and released were obtained using Equations (10) and (11) and included the contribution of the linear and nonlinear stiffness. The total stored energy from the experimental and analytical results as a function of the applied force were in good agreement, as shown in Figure 17. It can be observed that the stored elastic energy increased considerably in the nonlinear region as the applied force was increased. Hence, increasing the force increased the stretch–contraction in the hyperelastic material, and energy aggregation increased nonlinearly. Energy efficiency was approximately 68% for the maximum displacement of the entire system in the vertical bending configuration. Efficiency was calculated as the ratio of the energy released and injected. The energy dissipation can be attributed to the hyperelastic material's damping. Detailed discussion is provided in Section 6.2.

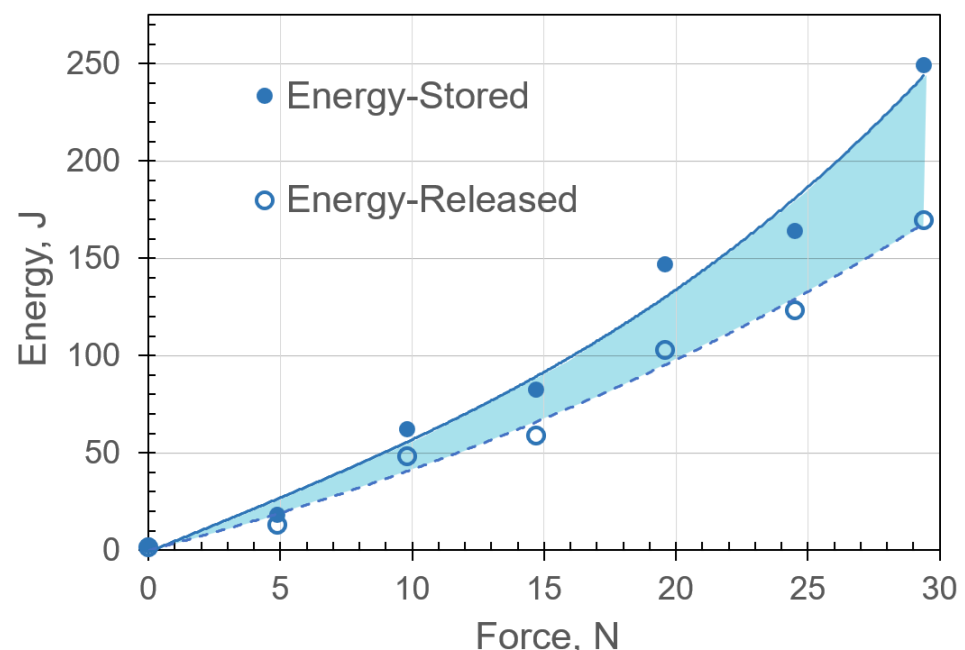


Figure 17. Total elastic energy storage for the musculoskeletal system in the bending load configuration. The energy released was the energy stored minus the energy dissipated. Experimental and analytical (from (11)) results are shown in markers and lines, respectively.

6.2. Elastic Energy Release

The resonance frequencies, f_r , due to the musculoskeletal system's free oscillation (undulation) motion at different applied loads were calculated and are shown in Figure 18. After inducing an impulse force, the system was free to undulate about the equilibrium position at its resonance frequency, which is the number of oscillations per second. Therefore, the resonance frequency was an ideal measure of the speed of undulation.

Free-oscillation-response data obtained from the modal impact experiments were recorded in the time domain and then transformed into the frequency domain [54,55]. The experiments were conducted for up to 200 Hz frequency with 0.5 Hz resolution. The natural frequency was estimated for the musculoskeletal system in two configurations: single- and double-sided tension of the soft materials, as shown in Figure 18. Applying tension force to the soft material caused contraction, which increased the resonance frequency (or equivalent stiffness).

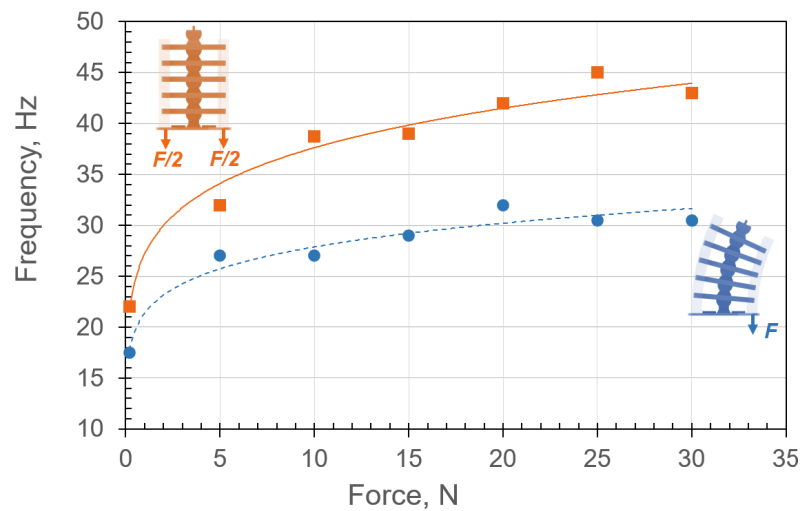


Figure 18. Undulation frequency for single- and double-sided tension configurations in blue and orange, respectively. The frequency appears to plateau asymptotically as the internal force is increased for both systems.

It can be concluded that increasing the tension in the muscles increases the undulation speed. For example, the undulation speed in the double-sided tension case was approximately 45 Hz due to applying a 29.4 N force, which meant that the system undulated with $2 \times 43 = 86$ center-crossings per second. In the absence of internal forces in the soft material, the undulation was $2 \times 22 = 44$ center-crossings per second. Note an initial increase in the force increased the undulation frequency significantly. However, the undulation frequency tended to plateau asymptotically as the internal force surged. This important finding indicates that the system is indeed nonlinear hybrid compliant, where the plateau is the softening–hardening transition in the stiffness (Figure 4). It is expected that a further increase in the applied force will cause the system to harden, and the force–displacement will become cubic (Figure 4). This behavior is consistent with the periodic motion seen in animals, where muscle stiffness varies to facilitate actuation over a broad natural frequency envelope [9]. The reason for actuating near or at the natural frequency is to maximize the response amplitude [56].

The corresponding damping due to applied forces in single-sided and double-sided tension configurations are reported in Figure 19. Both configurations show that an increase in the internal forces increased the overall structural damping. As expected, the system was highly damped due to energy absorption by the hyperelastic materials [6] and frictional forces between the joints [28]. For an applied internal force of 29.4 N in the single- and double-sided tension configurations, the damping ratios were approximately 32% and 42%, respectively. It is important to point out that the stiffness appeared to plateau asymptotically as the applied force was increased. While damping in Figure 19 appears to increase linearly, it should plateau as we increase the load, since it cannot continue this trend forever. The linear appearance could be due to the scatter in the data, which is common when estimating the damping of vibratory systems [37]. This behavior is also consistent with the soft material stress–strain response (Figure 12).

The damping ratios were utilized to estimate the energy dissipation (Figure 17). It can be observed that the release speed nearly doubled as the energy stored in the hyperelastic materials reached 250 J. This is consistent with the explosive motion of vertebral undulating animals.

Future research will include investigating the effects of geometric and material nonlinearity in various dynamic modes including steady-state motion. The goal is to understand the competing mechanisms between these nonlinearities, in which material nonlinearity tends to cause dynamic softening or compliance, and geometric nonlinearity promotes dynamic hardening [37]. The contribution of friction is another important topic that will be

addressed in future studies. More precisely, design principles are needed to describe the variation in friction due to tuning the structural stiffness with actuation forces.

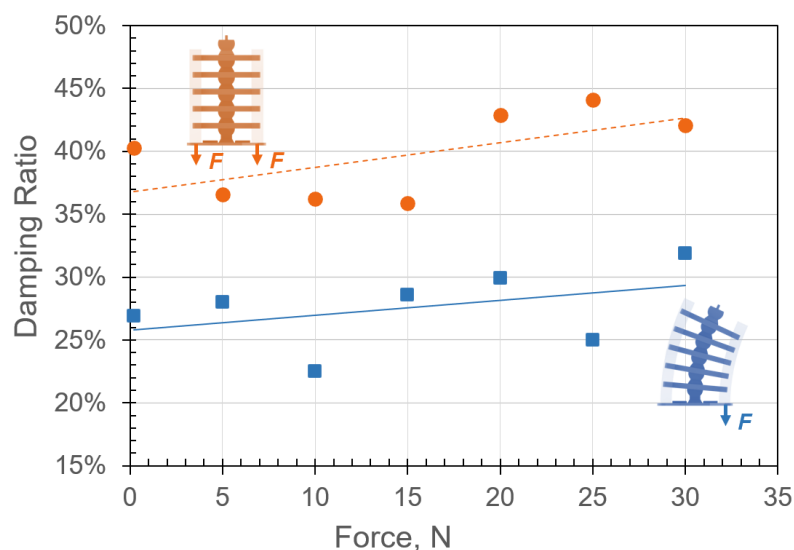


Figure 19. Damped undulation due to energy dissipation for single- and double-sided tension configurations in blue and orange, respectively. The damping ratio appears to increase linearly as the internal force is increased for both systems.

7. Conclusions

In this study, the mechanics of energy storage–release were demonstrated for a nature-inspired musculoskeletal system that consisted of 3D-printed rigid segments (bones) connected with soft hyperelastic material (muscles). The energy efficiency of the musculoskeletal system was approximately 68% to bend the structure from a vertical configuration to a 158 mm radius-of-curvature. Efficiency was defined as the ratio between the released and stored energy. Energy losses were attributed to the soft material’s high damping and to joint friction between the rigid segments in the musculoskeletal system. While contraction in the soft material increased by approximately 6%, an increase of more than 100% in the structural stiffness counteracted the negative effect of damping.

Nature-inspired musculoskeletal systems hold great promise as an alternative to current soft actuators that struggle to go beyond 30% energy efficiency. Combining rigid segments and soft materials in designing a musculoskeletal system was key to achieving these advantageous features. Utilizing 3D printing allowed us to easily apply geometric segmentation and nonlinear materials, as seen in nature, to demonstrate combined high elastic energy storage and range of motion in the system while maintaining structural stability.

Supplementary Materials: The following supporting information can be downloaded at: www.mdpi.com/xxx/s1. Video S1: Motion of the Musculoskeletal System, Video S2: Tracking the Deflection Motion, Code S3: Kinematics of the Musculoskeletal System.

Author Contributions: Conceptualization, P.W. and E.H.; methodology, P.W. and E.H.; software, P.W.; validation, P.W.; formal analysis, P.W. and E.H.; investigation, B.B., T.M. and E.H.; resources, P.W., A.S., B.B., T.M., S.F. and E.H.; data curation, P.W.; writing—original draft preparation, P.W., B.B. and E.H.; writing—review and editing, P.W., A.S., B.B., T.M., S.F. and E.H.; visualization, P.W., B.B. and E.H.; supervision, B.B. and E.H.; project administration, E.H.; funding acquisition, E.H. All authors have read and agreed to the published version of the manuscript.

Funding: This research received no external funding.

Data Availability Statement: The data presented in this study are available on request from the corresponding author. The data are not publicly available due to the large size of the files.

Acknowledgments: The authors would like to express their gratitude to Z.A.J. Lok of Twente University (Enschede, The Netherlands) for his assistance with the experimental design, instrumentation, and data collection, to Andre de Boer and Tiedo Tinga for their technical guidance, and to the members of the Design Lab at the University of Twente for providing access to the fabrication facilities and their expertise. Ed Habtour gratefully acknowledges the Engineer and Scientist Exchange Program (ESEP) funding provided by the Office of the Deputy Assistant Secretary of the United States Army for Defense Exports and Cooperation and the United States Army Research Laboratory, and the support of the Netherlands Organization for Applied Scientific Research.

Conflicts of Interest: The authors declare no conflict of interest.

References

1. Whitesides, G.M. Soft robotics. *Angew. Chem. Int. Ed.* **2018**, *57*, 4258–4273. [[CrossRef](#)] [[PubMed](#)]
2. Walker, J.; Zidek, T.; Harbel, C.; Yoon, S.; Strickland, F.S.; Kumar, S.; Shin, M. Soft robotics: A review of recent developments of pneumatic soft actuators. *Actuators* **2020**, *9*, 3. [[CrossRef](#)]
3. Zhou, L.Y.; Fu, J.; He, Y. A review of 3D printing technologies for soft polymer materials. *Adv. Funct. Mater.* **2020**, *30*, 2000187. [[CrossRef](#)]
4. Tawk, C.; Alici, G. A Review of 3D-Printable Soft Pneumatic Actuators and Sensors: Research Challenges and Opportunities. *Adv. Intell. Syst.* **2021**, *3*, 2000223. [[CrossRef](#)]
5. Pal, A.; Restrepo, V.; Goswami, D.; Martinez, R.V. Exploiting mechanical instabilities in soft robotics: Control, sensing, and actuation. *Adv. Mater.* **2021**, *33*, 2006939. [[CrossRef](#)]
6. Haghiastiani, G.; Habtour, E.; Park, S.H.; Gardea, F.; McAlpine, M.C. 3D printed electrically-driven soft actuators. *Extrem. Mech. Lett.* **2018**, *21*, 1–8. [[CrossRef](#)] [[PubMed](#)]
7. Qiu, Y.; Zhang, E.; Plamthottam, R.; Pei, Q. Dielectric elastomer artificial muscle: Materials innovations and device explorations. *Acc. Chem. Res.* **2019**, *52*, 316–325. [[CrossRef](#)] [[PubMed](#)]
8. Branyan, C.; Hatton, R.L.; Mengüç, Y. Snake-Inspired Kirigami Skin for Lateral Undulation of a Soft Snake Robot. *IEEE Robot. Autom. Lett.* **2020**, *5*, 1728–1733. [[CrossRef](#)]
9. Liu, Y.; Farimani, A.B. An Energy-Saving Snake Locomotion Gait Policy Using Deep Reinforcement Learning. *arXiv* **2021**, arXiv:2103.04511.
10. Hao, Z.; Song, S.; Li, B.; Jia, Q.X.; Zheng, T.; Zhang, Z. A Solvent Driven Dual Responsive Actuator based on MOF/Polymer Composite. *Sens. Actuators B Chem.* **2022**, *358*, 131448. [[CrossRef](#)]
11. Sim, H.J.; Kim, J.; Choi, C. Biomimetic Self-Powered Artificial Muscle Using Tri-Functional Yarns that Combine Generator, Supercapacitor, and Actuator Functions. *Sens. Actuators B Chem.* **2022**, *357*, 131461. [[CrossRef](#)]
12. Li, M.; Tang, Y.; Soon, R.H.; Dong, B.; Hu, W.; Sitti, M. Miniature coiled artificial muscle for wireless soft medical devices. *Sci. Adv.* **2022**, *8*, eabm5616. [[CrossRef](#)] [[PubMed](#)]
13. Bai, R.; Yang, J.; Suo, Z. Fatigue of hydrogels. *Eur. J. Mech. A Solids* **2019**, *74*, 337–370. [[CrossRef](#)]
14. Al-Rubaiai, M.; Pinto, T.; Qian, C.; Tan, X. Soft actuators with stiffness and shape modulation using 3D-printed conductive polylactic acid material. *Soft Robot.* **2019**, *6*, 318–332. [[CrossRef](#)] [[PubMed](#)]
15. Zhu, J.; Lyu, L.; Xu, Y.; Liang, H.; Zhang, X.; Ding, H.; Wu, Z. Intelligent Soft Surgical Robots for Next-Generation Minimally Invasive Surgery. *Adv. Intell. Syst.* **2021**, *3*, 2100011. [[CrossRef](#)]
16. Li, X.; Duan, H.; Lv, P.; Yi, X. Soft actuators based on liquid–vapor phase change composites. *Soft Robot.* **2021**, *8*, 251–261. [[CrossRef](#)]
17. Xavier, M.S.; Fleming, A.J.; Yong, Y.K. Finite element modeling of soft fluidic actuators: Overview and recent developments. *Adv. Intell. Syst.* **2021**, *3*, 2000187. [[CrossRef](#)]
18. Chung, H.J.; Parsons, A.M.; Zheng, L. Magnetically controlled soft robotics utilizing elastomers and gels in actuation: A review. *Adv. Intell. Syst.* **2021**, *3*, 2000186. [[CrossRef](#)]
19. Zhang, Y.F.; Zhang, N.; Hingorani, H.; Ding, N.; Wang, D.; Yuan, C.; Zhang, B.; Gu, G.; Ge, Q. Fast-response, stiffness-tunable soft actuator by hybrid multimaterial 3D printing. *Adv. Funct. Mater.* **2019**, *29*, 1806698. [[CrossRef](#)]
20. Nassour, J.; Zhao, G.; Grimmer, M. Soft pneumatic elbow exoskeleton reduces the muscle activity, metabolic cost and fatigue during holding and carrying of loads. *Sci. Rep.* **2021**, *11*, 12556. [[CrossRef](#)]
21. Sun, J.; Zhang, D.; Zhang, Y.; Zhu, X.; Xi, J.; Zhang, Y.D. Research on performance of rigid-hoop-reinforced multi-DOF soft actuator. *Adv. Mech. Eng.* **2021**, *13*, 16878140211026718. [[CrossRef](#)]
22. Jayne, B.C. What defines different modes of snake locomotion? *Integr. Comp. Biol.* **2020**, *60*, 156–170. [[CrossRef](#)] [[PubMed](#)]
23. Seetohul, J.; Shafiee, M. Snake Robots for Surgical Applications: A Review. *Robotics* **2022**, *11*, 57.
24. Li, X.; Ren, C.; Ma, S. Optimal Path Following Control With Efficient Computation for Snake Robots Subject to Multiple Constraints and Unknown Frictions. *IEEE Robot. Autom. Lett.* **2022**, *7*, 9151–9158. [[CrossRef](#)]
25. Ramesh, D.; Fu, Q.; Li, C. SenSnake: A snake robot with contact force sensing for studying locomotion in complex 3-D terrain. In Proceedings of the 2022 International Conference on Robotics and Automation (ICRA), Philadelphia, PA, USA, 23–27 May 2022; pp. 2068–2075.

26. Wang, C.; Puranam, V.R.; Misra, S.; Venkiteswaran, V.K. A Snake-Inspired Multi-Segmented Magnetic Soft Robot towards Medical Applications. *IEEE Robot. Autom. Lett.* **2022**, *7*, 5795–5802. [[CrossRef](#)]
27. Feng, Y.; Siegmund, T.; Habtour, E.; Riddick, J. Impact Mechanics of Topologically Interlocked Material Assemblies. *Int. J. Impact Eng.* **2015**, *75*, 140–149. [[CrossRef](#)]
28. Siegmund, T.; Barthelat, F.; Cipra, R.; Habtour, E.; Riddick, J. Manufacture and mechanics of topologically interlocked material assemblies. *Appl. Mech. Rev.* **2016**, *68*, 040803. [[CrossRef](#)]
29. Jurestovsky, D.J.; Jayne, B.C.; Astley, H.C. Experimental modification of morphology reveals the effects of the zygosphenes-zygantrum joint on the range of motion of snake vertebrae. *J. Exp. Biol.* **2020**, *223*, jeb216531. [[CrossRef](#)]
30. Li, D.; Wang, C.; Deng, H.; Wei, Y. Motion Planning Algorithm of a Multi-Joint Snake-Like Robot Based on Improved Serpenoid Curve. *IEEE Access* **2020**, *8*, 8346–8360. [[CrossRef](#)]
31. Virgala, I.; Kelemen, M.; Prada, E.; Sukop, M.; Kot, T.; Bobovský, Z.; Varga, M.; Ferenčík, P. A snake robot for locomotion in a pipe using trapezium-like travelling wave. *Mech. Mach. Theory* **2021**, *158*, 104221. [[CrossRef](#)]
32. Bolmin, O.; Socha, J.J.; Alleyne, M.; Dunn, A.C.; Fezzaa, K.; Wissa, A.A. Nonlinear elasticity and damping govern ultrafast dynamics in click beetles. *Proc. Natl. Acad. Sci. USA* **2021**, *118*, e2014569118. [[CrossRef](#)] [[PubMed](#)]
33. Han, B.; Ma, Z.C.; Zhang, Y.L.; Zhu, L.; Fan, H.; Bai, B.; Chen, Q.D.; Yang, G.Z.; Sun, H.B. Reprogrammable Soft Robot Actuation by Synergistic Magnetic and Light Fields. *Adv. Funct. Mater.* **2022**, *32*, 2110997. [[CrossRef](#)]
34. Ruan, Y.; Zhang, M.; Kundrata, R.; Qiu, L.; Ge, S.; Yang, X.; Chen, X.; Jiang, S. Functional Morphology of the Thorax of the Click Beetle *Campsolesternus auratus* (Coleoptera, Elateridae), with an Emphasis on Its Jumping Mechanism. *Insects* **2022**, *13*, 248. [[CrossRef](#)] [[PubMed](#)]
35. Aliev, A.E.; Mayo, N.K.; Baughman, R.H.; Mills, B.T.; Habtour, E. Subwoofer and nanotube butterfly acoustic flame extinction. *J. Phys. D Appl. Phys.* **2017**, *50*, 29LT01. [[CrossRef](#)]
36. Peele, B.; Li, S.; Larson, C.; Cortell, J.; Habtour, E.; Shepherd, R. Untethered stretchable displays for tactile interaction. *Soft Robot.* **2019**, *6*, 142–149. [[CrossRef](#)] [[PubMed](#)]
37. Habtour, E.; Di Maio, D.; Masmeyer, T.; Cordova Gonzalez, L.; Tinga, T. Highly Sensitive Nonlinear Identification to Track Early Fatigue Signs in Flexible Structures. *J. Nondestruct. Eval. Diagn. Progn. Eng. Syst.* **2022**, *5*, 021005. [[CrossRef](#)]
38. Bolmin, O.; Wei, L.; Hazel, A.M.; Dunn, A.C.; Wissa, A.; Alleyne, M. Latching of the click beetle (Coleoptera: Elateridae) thoracic hinge enabled by the morphology and mechanics of conformal structures. *J. Exp. Biol.* **2019**, *222*, jeb196683. [[CrossRef](#)]
39. Yeaton, I.J.; Ross, S.D.; Baumgardner, G.A.; Socha, J.J. Undulation enables gliding in flying snakes. *Nat. Phys.* **2020**, *16*, 974–982. [[CrossRef](#)]
40. Gerald, G.W. Effects of morphology, substrate use, and potential trade-offs on locomotor performance during multiple modes of snake locomotion. *Evol. Ecol. Res.* **2017**, *18*, 601–620.
41. Chun, H.T.D.; Roberts, J.O.; Sayed, M.E.; Aracri, S.; Stokes, A.A. Towards more energy efficient pneumatic soft actuators using a port-hamiltonian approach. In Proceedings of the 2019 2nd IEEE International Conference on Soft Robotics (RoboSoft), Seoul, Korea, 14–18 April 2019; pp. 277–282.
42. Chen, Y.; Yang, J.; Zhang, X.; Feng, Y.; Zeng, H.; Wang, L.; Feng, W. Light-driven bimorph soft actuators: Design, fabrication, and properties. *Mater. Horiz.* **2021**, *8*, 728–757. [[CrossRef](#)]
43. Bell, M.A.; Gorissen, B.; Bertoldi, K.; Weaver, J.C.; Wood, R.J. A Modular and Self-Contained Fluidic Engine for Soft Actuators. *Adv. Intell. Syst.* **2022**, *4*, 2100094. [[CrossRef](#)]
44. Eutioonat-Diffo, P.A.; Chen, Y.; Guan, J.; Cayla, A.; Campagne, C.; Zeng, X.; Nierstrasz, V. Stress, strain and deformation of poly-lactic acid filament deposited onto polyethylene terephthalate woven fabric through 3D printing process. *Sci. Rep.* **2019**, *9*, 14333. [[CrossRef](#)]
45. Vasiliev, V.V.; Morozov, E.V. *Advanced Mechanics of Composite Materials and Structural Elements*; Elsevier: Amsterdam, The Netherlands, 2013.
46. Owolabi, G.; Peterson, A.; Habtour, E.; Riddick, J.; Coatney, M.; Olasumboye, A.; Bolling, D. Dynamic response of acrylonitrile butadiene styrene under impact loading. *Int. J. Mech. Mater. Eng.* **2016**, *11*, 1–8. [[CrossRef](#)]
47. Kim, Y.J.; Cheng, S.; Kim, S.; Iagnemma, K. A stiffness-adjustable hyperredundant manipulator using a variable neutral-line mechanism for minimally invasive surgery. *IEEE Trans. Robot.* **2014**, *30*, 382–395. [[CrossRef](#)]
48. Melly, S.K.; Liu, L.; Liu, Y.; Leng, J. Improved Carroll's hyperelastic model considering compressibility and its finite element implementation. *Acta Mech. Sin.* **2021**, *37*, 785–796. [[CrossRef](#)]
49. Habtour, E.M.; Cole, D.P.; Kube, C.M.; Henry, T.C.; Haynes, R.A.; Gardea, F.; Sano, T.; Tinga, T. Structural state awareness through integration of global dynamic and local material behavior. *J. Intell. Mater. Syst. Struct.* **2019**, *30*, 1355–1365. [[CrossRef](#)]
50. Ernst, M.; Habtour, E.; Dasgupta, A. Examining Steinberg's Octave rule applicability for electronic systems exposed to multiaxial vibration. *IEEE Trans. Compon. Packag. Manuf. Technol.* **2016**, *6*, 561–568. [[CrossRef](#)]
51. Habtour, E.; Paulus, M.; Dasgupta, A. Modeling approach for predicting the rate of frequency change of notched beam exposed to Gaussian random excitation. *Shock Vib.* **2014**, *2014*, 164039. [[CrossRef](#)]
52. Rao, S.S. *Vibration of Continuous Systems*; John Wiley & Sons: Hoboken, NJ, USA, 2019.
53. Paulus, M.; Dasgupta, A.; Habtour, E. Life estimation model of a cantilevered beam subjected to complex random vibration. *Fatigue Fract. Eng. Mater. Struct.* **2012**, *35*, 1058–1070. [[CrossRef](#)]

-
54. Montoya, A.; Habtour, E.; Moreu, F. Quantifying Information without Entropy: Identifying Intermittent Disturbances in Dynamical Systems. *Entropy* **2020**, *22*, 1199. [[CrossRef](#)]
 55. Montoya, A.; Habtour, E.; Moreu, F. Detecting hidden transient events in noisy nonlinear time-series. *Chaos Interdiscip. J. Nonlinear Sci.* **2022**, *32*, 073131. [[CrossRef](#)] [[PubMed](#)]
 56. Habtour, E.; Sridharan, R.; Dasgupta, A.; Robeson, M.; Vantadori, S. Phase influence of combined rotational and transverse vibrations on the structural response. *Mech. Syst. Signal Process.* **2018**, *100*, 371–383. [[CrossRef](#)]